

pubs.acs.org/acsaelm Article

# Molecularly Engineered Quinoxaline-Pyridyl Pyrazine Polymers for Field-Effect Transistors and Complementary Circuits

John Barron, Salahuddin Attar, Arash Ghobadi, Shubhra Gangopadhyay, Dusan Sredojevic, Mohammed Al-Hashimi,\* and Suchismita Guha\*



Cite This: ACS Appl. Electron. Mater. 2024, 6, 1464-1474



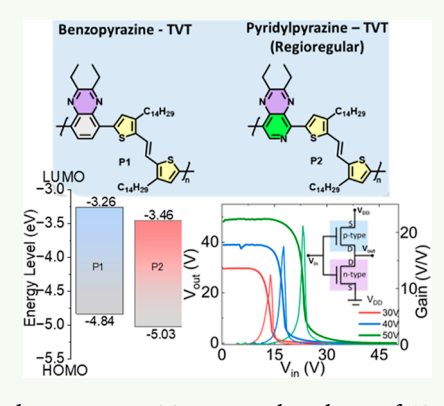
**ACCESS** I

III Metrics & More

Article Recommendations

s Supporting Information

**ABSTRACT:** Regioregularity in conjugated polymers plays a significant role in enhancing the semiconducting properties and narrowing the optical band gap. Two donor—acceptor copolymers, specifically quinoxaline-thienylenevinylene (P1) and regioregular pyridyl pyrazine-thienylenevinylene (P2), were synthesized and characterized. Their potential applications in organic field-effect transistors (FETs) and complementary inverter circuits were explored. P2 exhibits a narrower absorption spectrum with distinct vibronic peaks compared to P1. In both top-gate and bottom-gate FET architectures, the copolymers display p-type behavior, with P2 demonstrating approximately an order of magnitude higher carrier mobility ( $\sim 10^{-3} \text{ cm}^2/(\text{V s})$ ) than P1. The performance of the FETs is further improved by the surface treatment of the source—drain contacts, which is particularly noticeable in P1. These p-type FETs, incorporating P1 and P2, were employed in complementary voltage inverter circuits along with thiazole-selenophene-linked fluorinated isoindigo (IID-TzSe) n-type organic FETs. The P1–IID-



TzSe inverter, characterized by balanced p- and n-channels with similar threshold voltages, shows a gain >20 at a supply voltage of 50 V. Similar gains are also observed in the P2-IID-TzSe inverter circuits.

**KEYWORDS:** donor—acceptor copolymer, field-effect transistor, current—voltage characteristics, complementary circuits, dielectric, density functional theory

#### 1. INTRODUCTION

Being able to tune the electronic and optical properties with electron-rich and electron-deficient units connected through a covalent linkage in donor-acceptor (D-A)-type copolymers has been very attractive for expanding the scope of low-cost electronic devices. 1-5 Not only do D-A copolymers help in reducing the optical band gap, which have excellent opportunities in photovoltaics, 6,7 having donor and acceptor chromophores in a polymer chain also enables both p-type and n-type transport. 5,8 Electron-deficient acceptor units such as benzothiadiazole (BT), benzotriazole (BTr), diketopyrrolopyrrole (DPP), isoindigo (IID), and naphthalenediimide (NDI) have received a lot of interest in organic electronics. DPP-based copolymers have been attractive in organic solar cells, photodetectors, and transistors due to their high carrier mobilities.<sup>9-13</sup> Replacing the sulfur atom with other heavier atoms offers a versatile approach for tailoring the electronic properties of materials 14 and enhancing charge transport properties in IID-based copolymers. 15-17 NDI-type copolymers show great potential for doping and have found applications in various electronic devices, including thermoelectrics. 18-20

In conjunction with electron-rich donor units such as fluorene, carbazole, thiophene, bithiophene, and benzodithiophene, acceptor units such as benzothiazole, benzothiadiazole,

and quinoxaline have been attractive for optoelectronic applications. <sup>21–23</sup> In particular, the quinoxaline (Qx)- and pyridyl pyrazine (PyPyz)-based systems, which may be synthesized using low-cost starting materials in high yields and are highly stable under ambient conditions, are key players in a new generation of bulk heterojunction-type organic solar cells. <sup>23–26</sup> There are few reports of Qx- or PyPyz-based copolymers in transistor applications, <sup>27</sup> and donor—acceptor copolymers (Figure 1) with acceptor units such as BT, <sup>28</sup> BTr, <sup>29</sup> and pyridyl thiadiazole <sup>30</sup> that have achieved high performance in ambipolar transistors. <sup>31</sup>

Other molecular design strategies known from homopolymers such as poly(3-hexylthiophene) (P3HT) involve regioregularity which impacts the electronic and optical properties. Regioregular (RR) P3HT with its head-to-tail alkyl-chain conformation displays a planar backbone, which is responsible for structural homogeneity and high crystallinity. Regioregularity has also been explored in D–A copolymers

Received: December 19, 2023 Revised: February 7, 2024 Accepted: February 8, 2024 Published: February 16, 2024





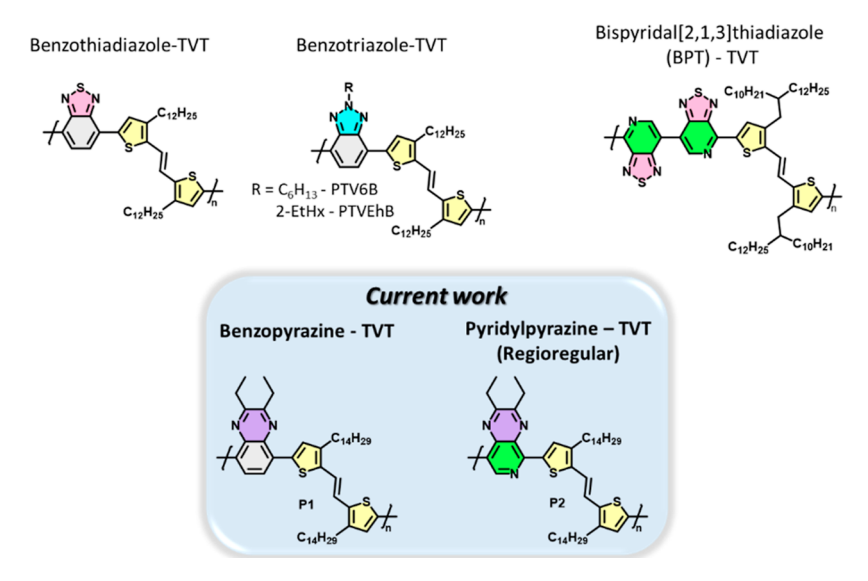


Figure 1. Structures of donor-acceptor polymers of TVT with BT, BTr, bispyridyl thiadiazole reported in the literature and current work with benzopyrazine and pyridyl pyrazine copolymers.

where either the D or A (or both) copolymers are asymmetric. In benzothiadiazole acceptor-type units, a carbon atom is often replaced by nitrogen (N) to obtain a pyridyl thiadiazole unit, resulting in a planar quinoidal backbone with increased electron affinity. Onsequently, record ambipolar transport with hole and electron mobilities up to 6.9 and 8.5 cm $^2/(V s)$ has been reported by increasing the acceptor unit in bispyridyl thiadiazole-thienylenevinylene (TVT) copolymers (Figure 1).31 Schemes for achieving planar backbones in D-A copolymers have incorporated molecular-engineered donor units such as TVT derivatives. With BTr as the acceptor unit, the vinyl linkage in the TVT units reduces the angular torsion on successive aromatic rings. TVT-BTr-based D-A copolymers (Figure 1) exhibit enhanced charge transport properties in field-effect transistors (FETs) with carrier mobilities in the range of  $1.5-2.5 \text{ cm}^2/(\text{V s})^{29}$  Equally important in the area of organic electronics is the search for low-cost materials. For basic digital circuits, carrier mobility is not the only criterion, but well-balanced p- and n-channels are more pertinent. With this in mind, we have designed D-A systems using low-cost starting materials for applications in basic complementary voltage inverter circuits.

In this study, we have synthesized two new copolymers by incorporating Qx and PyPyz units with TVT units, resulting in systems that differ solely in the presence of an additional electronegative N atom. We successfully synthesized copolymers P1 and P2, which consist of TVT-Qx repeating units and TVT-PyPyz repeating units, respectively. P2 was synthesized with the specific aim of achieving a regioregular conformation of the pyridyl pyrazine units, providing a mechanism to eliminate any potential influence from other isomeric or random backbone arrangements and ensuring the desired structural integrity of the copolymer. To showcase their suitability in electronic devices, we fabricated FETs using two different configurations: top-gate bottom contact (TGBC) with a poly(methyl methacrylate) (PMMA) dielectric layer, and bottom-gate top contact (BGTC) with a SiO<sub>2</sub> dielectric layer. Both P1 and P2 FETs exhibit a p-type behavior, with carrier mobilities ranging from  $10^{-3}$  to  $10^{-4}$  cm<sup>2</sup>/(V s). On average, P2 demonstrates better FET performance compared with P1. Interestingly, we observed that treating the Au

source/drain contacts with a self-assembled monolayer (SAM) leads to further improvement in the performance of P1 FETs. However, since P2 has a deeper highest occupied molecular orbital (HOMO) level by approximately 0.2 eV compared to P1, surface treatments of the contacts do not affect the FET properties in P2. Notably, the p-type FETs were configured in complementary voltage inverter circuits. Our prior work demonstrated Se-substituted thiazole-flanked fluorinated IID copolymer (IID-TzSe) to be ambipolar with exclusively n-type transport in TGBC FET architectures. 17 Using IID-TzSe as the n-channel FET, both P1 and P2 FETs show promising gain in inverter circuits. The HOMO and lowest unoccupied molecular orbital (LUMO) (lowest occupied molecular orbital) levels of IID-TzSe better matched with P1 due to which the complementary inverter circuit shows an ideal push-pull-type behavior. Using an analytical model, we simulate the inverter characteristics for P1-IID-TzSe. Inverter characteristics with P2 and IID-TzSe show a slight deviation from the ideal behavior. We further compare a DPP-based copolymer in conjunction with IID-TzSe in inverter circuits to understand the nonideal nature of the inverter circuits. Designing Qx and PyPyz with coplanar donor units such as TVT opens their application not just in thin-film transistors, but combining with other D-A IID-based n-type FETs has promising applications in digital electronic circuits.

#### 2. EXPERIMENTAL SECTION

**2.1. Materials.** All commercially available solvents were distilled and freshly dried by standard drying methods. Reagents and chemicals were used as received without further purification unless otherwise stated. 3,6-Dibromobenzene-1,2-diamine (1) and hexane-3,4-diamine (2) was prepared **according** to the reported procedure. (E)-1,2-Bis(3-tetradecyl-5-(trimethylstannyl)thiophen-2-yl)ethene was purchased from Solarmer Inc. Unless otherwise stated, all operations and reactions were carried out under argon using standard Schlenk line techniques. IID-TzSe was synthesized according to the reported procedure. Analytical thin-layer chromatography was performed on Merck aluminum-backed plates precoated with silica (0.2 mm, 60 F254) gel. Plates were visualized by exposure to UV light (254 nm or 365 nm). The copolymer of DPP (DPP-DTT) was purchased from 1-Material Inc. (Dorval, Quebec, Canada).

Scheme 1. Synthetic Route to Monomers: M1, M2, and Copolymers: P1, Regioregular P2, and Their Dilute Solutions in Chlorobenzene (Top Right)

**2.2. Synthesis.** 2.2.1. Monomer Synthesis. The synthetic pathway for the preparation of monomers M1 and M2 is illustrated in Scheme 1. Upon refluxing in ethanol, 3,6-dibromobenzene-1,2-diamine (1) or 2,5-dibromopyridine-3,4-diamine (2) underwent a dehydrative cyclization reaction with hexane-3,4-dione (3), yielding two monomers, namely, 5,8-dibromo-2,3-diethylquinoxaline (M1) and 5,8-dibromo-2,3-diethylpyrido[3,4-b]pyrazine (4).

The synthesis of regioregular pyridyl pyrazine polymers is based on the chemistry of 5,8-dibromo-2,3-diethylpyrido[3,4-b]pyrazine (4). Owing to the reactivity of 2,5-dibromopyridine, it is projected that Pd-mediated Stille cross-coupling of (4) with stannylated aromatic compounds would preferentially occur at C–Br adjacent to the pyridal N atom. Cross-coupling of (E)-1,2-bis(3-tetradecyl-5-(trimethylstannyl)thiophen-2-yl)ethene (5) and (4) in the presence of Tetrakis(triphenylphosphine)palladium(0) affords the monomer (E)-1,2-bis(5-(8-bromo-2,3-diethylpyrido[3,4-b]pyrazin-5-yl)-3-tetradecylthiophen-2-yl)ethene (M2) in yields reaching 90%. This synthetic approach ensures a favorable arrangement of pyridyl pyrazine structural units along the polymer backbone, resulting in regioregularity.

2.2.2. Polymer Synthesis. As shown in Scheme 1, copolymers P1 and P2 were prepared via microwave-assisted Stille coupling of M1 and M2 in chlorobenzene (5), with Tetrakis(triphenylphosphine) palladium(0) as a catalyst. The polymers were precipitated in acidified methanol and purified via Soxhlet extraction with a sequence of refluxing methanol, acetone, and n-hexane and chloroform. Finally, the polymers were extracted by refluxing chlorobenzene. The solvent was removed, and P1 and P2 were dissolved in chlorobenzene, which were further reprecipitated in 50% acetone in methanol, filtered, and isolated as dark solids. Gel permeation chromatography (GPC) yielded the polydispersity index (D) and the number-average molecular weight  $(M_n)$  of the polymers. Accordingly, a chlorobenzene solution with polystyrene standards at 85 °C was used as the calibrant. The  $M_n$  values of copolymers P1 and P2 were measured to be 108 and 150 kDa, respectively, with D in the range of 1.6-2.25 (Figures S1 and S2). Table 1 summarizes the physical, electrochemical, and optical properties of P1 and P2.

**2.3. FET and Complementary Voltage Inverter Development.** The FETs were fabricated in two different staggered architectures: BGTC and TGBC. Details of FET fabrication are provided in Supporting Information. The individual TGBC FETs utilizing P1/P2 or IID-TzSe as the semiconducting layer (with PMMA as the dielectric) were interconnected to form an inverter circuit architecture. The thickness of the top PMMA dielectric layer was approximately 125 nm. The P1/P2 devices (p-type) act as the "pull-up" FET and the IID-TzSe device acts as the "pull-down" FET.

In this way, the source contact of the P1/P2 FET was connected to the supply voltage of the inverter, and the source contact of the IID-TzSe FET was connected to the ground. A solder was used to form a connected drain contact for each device, through which the output signal could be measured. Similarly, a solder was used to connect the gate contacts for each device, through which the input signal could be applied.

**2.4. Electrical Characterization.** The output and transfer characteristics of the FETs were measured using a combination of Keithley 2400 and Keithley 236 source meters. The output characteristics were determined by sweeping the source—drain bias  $(V_{\rm DS})$  and measuring the source—drain current  $(I_{\rm D})$  for a given gate—source bias  $(V_{\rm GS})$ . The transfer measurements were conducted in the saturation region by sweeping  $V_{\rm GS}$  while holding  $V_{\rm DS}$  constant. The transfer measurements yielded pertinent device characteristics such as charge carrier mobility, the on/off ratio, and threshold voltage  $(V_{\rm Th})$ . The carrier mobility  $(\mu)$  was extracted from the saturation region of the transfer characteristics. With  $C_{\rm i}$  being the dielectric capacitance, W the channel width, and W the channel length, the saturation region  $W = \frac{2L}{WC_{\rm i}} \left(\frac{\partial \sqrt{I_{\rm D}}}{\partial V_{\rm GS}}\right)^2$ . All measurements were performed under ambient

conditions.

To perform the voltage transfer characteristics of the inverter circuit, Keithley 2400 and Keithley 236 source meters were used. An additional Keithley 2400 source meter (referred to hereafter as

circuit, Keithley 2400 and Keithley 236 source meters were used. An additional Keithley 2400 source meter (referred to hereafter as Keithley 2400-EXT) was utilized for applying the supply voltage  $(V_{\rm DD})$  to the circuit. Keithley 2400 applies a common  $V_{\rm in}$  to the gate of each FET; Keithley 2400-EXT applies  $V_{\rm DD}$  to the source contact of the p-type (pull-up) FET, and Keithley 236 measures  $V_{\rm out}$  through the common (soldered) connection between each of the device drain contacts. Each of the source meters shares a common ground, which is connected to the source contact of the n-type (pull-down) FET.

## 3. RESULTS AND DISCUSSION

**3.1. Optical, Electrochemical, and Thermal Properties.** The ultraviolet–visible (UV–vis) absorption spectra of **P1** and **P2** were obtained from both chlorobenzene solutions and thin films, as shown in Figure 2a,b. The  $\pi$ – $\pi$ \* localized electronic transitions of the conjugated moieties were recorded around 400 nm for both polymer films. The charge transfer peak in the range of 500–800 nm shows two apparent vibronic bands at higher (0–1) and lower (0–0) energies, which are normally attributed to polymer aggregation. The absorption spectrum of **P1** in the solution phase depicts one main

Table 1. Physical, Electrochemical, and Optical Characteristics of Copolymers P1 and P2

polymer	$M_{\rm n}~({ m kDa})^a$	$\mathbf{P}_{\boldsymbol{b}}$	$T_{ m d}$ (°C) $^c$	$\lambda_{ ext{max}}^{ ext{ sol }} ( ext{nm})^d$	$\lambda_{ ext{max}}^{ ext{film}}  ext{(nm)}^e$	HOMO (eV)	LUMO (eV) $E_{\rm g}^{\rm el}$ (eV) <sup>f</sup>		$E_{ m g}^{ m opt}~({ m eV})^{\cal g}$	Lamellar $d$ (Å) <sup><math>h</math></sup>	$\pi - \pi d (Å)^i$	$RMS (nm)^j$
P1	108	1.6	320	602	615, 658	-4.84	-3.26	1.58	1.57	21.96	3.70	3.19
P2	150	2.2	295	656, 715	646, 706	-5.03	-3.46	1.57	1.60	24.79	3.64	1.39
<sup>a</sup> Number-av	erage molecular robenzene. <sup>e</sup> Ma	r weight d	etermined by	<sup>a</sup> Number-average molecular weight determined by GPC (against polystoek in chlorobenzene. <sup>a</sup> Maximum absorption peak for a spin-coated	25	ls) in chlorobenze	energy. <sup>8</sup> Optical	lydispersity index band gap energy	t. <sup>c</sup> Thermal d	yrene standards) in chlorobenzene at 85 °C. $^b$ Polydispersity index $^c$ Thermal decomposition temperature. $^d$ Maximum absorption film. $^f$ Electrochemical band gap energy. $^g$ Optical band gap energy. $^h$ Lamellar $^d$ -spacing from X-ray diffraction. $^t$ $^t$ $^t$ stacking $^d$ -	erature. <sup>d</sup> Maxim v diffraction. <sup>i</sup> $\pi$	um absorption $-\pi$ stacking $d$ -

spacing from X-ray diffraction. /Root-mean-square roughness of polymer films from atomic force measurements.

absorption band with maxima at 602 nm; in the solid-state, it is red-shifted to 615 nm (corresponding to the (0-1) transition). A less pronounced (0-0) transition around 658 nm arises due to a strong intermolecular aggregation from the interchain  $\pi - \pi^*$  transition. **P2** exhibits two absorbance maxima at 656 and 715 nm in the solution phase; however, the film shows slightly blue-shifted absorption peaks at 646 and 706 nm. A clear broadening of absorption spectrum with a clear increase in the (0-1) peak intensity in the solid-state absorption of P2 may be tentatively attributed to the aggregation intermediate between H-type and J-type.<sup>35</sup> The optical band gaps (E<sub>g</sub> opt) were calculated from the onsets of the absorption spectra in the thin films and were found to be 1.57 and 1.60 eV for P1 and P2, respectively. This small difference in the optical band gap energy suggests that the inclusion of the N-atom in the PyPyz polymeric backbone mostly affects the absorption spectrum profile and its aggregation behavior. Similar observations have been reported in pyridal thidiazole copolymers.30

Cyclic voltammetry (CV) measurements (Figure 2c) reveal the influence of the polymer structure on the frontier molecular orbitals (Figure 2d). The results are tabulated in Table 1. The LUMO energy was extracted by subtracting the optical band gap energy from the HOMO energy level because of unclear reduction peaks. P1 exhibits  $E_{\text{LUMO}} \approx -3.26$  eV, while P2 displayed a slightly deeper  $E_{\text{LUMO}} \approx -3.46$  eV. We attribute this difference to the LUMO level residing mostly in the electron-withdrawing quinoxaline or pyridyl pyrazine units in P2. However, the HOMO is raised in energy by  $\sim 0.19$  eV for P1 ( $E_{\text{HOMO}} = -4.84 \text{ eV}$ ) relative to P2 ( $E_{\text{HOMO}} = -5.03$ eV), which may be due to the more ordered Qx orientation compared to the PyPyz unit, and as a result improving the HOMO wave function delocalization along the polymer backbone. Thus, the introduction of an electronegative Natom along the polymeric backbone leads to a lowering of both the HOMO and LUMO energy levels, highlighting increased stability and consequently reduced oxidative potential. Although the accurate determination of  $E_{\text{HOMO}}$  and  $E_{\text{LUMO}}$ from CV measurements poses inherent challenges, it is noteworthy that the band gap energies derived from electrochemical measurements show a strong correlation with those obtained from optical spectroscopy.

Thermogravimetric analysis and differential scanning calorimetry (DSC) under nitrogen atmosphere were used to determine the thermal properties of the polymers. As shown in Figure S3 and Table 1, copolymers P1 and P2 exhibited comparable thermal stability below 300 °C. Distinct onset decomposition temperatures  $(T_d)$  of 320 and 295 °C were observed for P1 and P2, respectively. We attribute this difference to the lower electronic stability of P2 due to the presence of an additional electronegative N atom along the conjugated backbone unit. Furthermore, P1 exhibited a weight loss of approximately 4% at around 347 °C, while P2 displayed a double weight loss of 10% at 337 °C. The DSC results (Figure S4) indicated that neither polymer showed any melting temperature peaks from room temperature up to 350 °C, suggesting the amorphous nature of both polymers. This behavior arises due to the planarity of their similar polymeric backbones, restricting molecular mobility. These observations align with the findings reported for similar copolymers in the literature. 15

3.2. Density Functional Theory Results. The electronic ground states of the two polymers were optimized via density

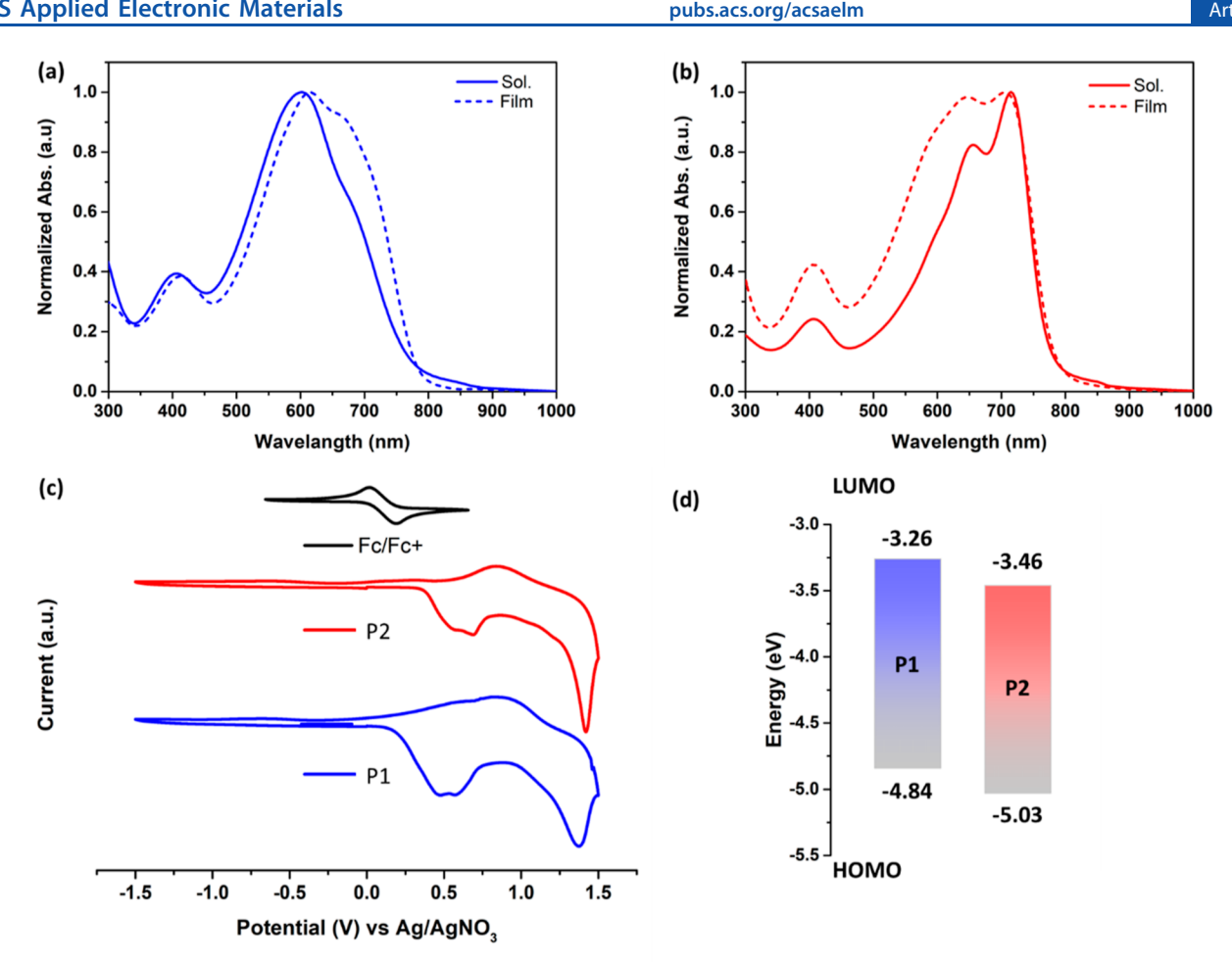


Figure 2. (a,b) UV-vis absorption spectra in chlorobenzene solution and from thin films of P1 and P2, respectively. (c) CV and (d) HOMO-LUMO levels of P1 (red) and P2 (blue).

functional theory (DFT) calculations using the B3LYP hybrid functional<sup>36,37</sup> with the 6-31G(d,p) basis set,<sup>38</sup> as implemented in the Gaussian 09 program.<sup>39</sup> Subsequent frequency calculations resulted in optimized geometries representing the true minima. To reduce the computational burden, the thiophene, benzopyrazine, and pyridyl pyrazine alkyl side chains were converted to methyl groups. The optimized geometries of P1 and P2 dimeric structures and the spatial distributions of the frontier molecular orbitals are shown in Figure 3. The HOMO/LUMO wave functions of both structures reveal that the molecular orbitals are well delocalized over the entire quinoxaline-TVT (P1) and pyridyl pyrazine-TVT (P2)-conjugated linear arrays (Figure 3).

The optimized tetrameric structure of the P2 copolymer is almost perfectly planar, with the torsion angles between consecutive pyridyl pyrazine/TVT units ranging from 0 to 4°. At variance, the optimized dimeric structure of P1 displays a higher deviation from planarity, with the torsion angle values reaching 24° (Figure 3). The higher planarity of P2 may be rationalized through the difference between benzo- and pyridyl-pyrazine units; the latter allows a large number of intramolecular contacts of the N-pyridyl atoms. The interatomic contacts between the sulfur (thiophene) and nitrogen atoms of (pyridyl)pyrazine, spanning from 2.80 to 2.86 Å, are all shorter than the sum of van der Waal radii of S and N atoms (1.80 and 1.55 Å, respectively), indicating the stabilizing nature of noncovalent interactions. 40 The DFT

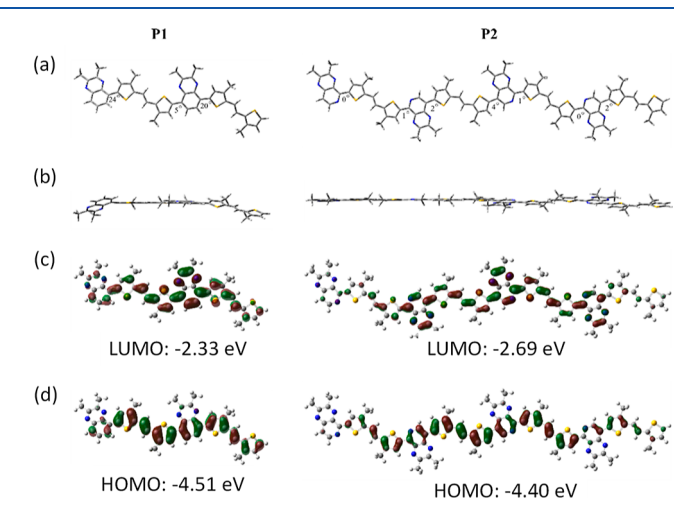


Figure 3. Optimized dimeric structures representing polymers P1 and P2, respectively: (a) top and (b) side views. The LUMO (c) and HOMO (d) orbitals of the dimers are shown.

calculations reveal that the P1 structure can exist in two conformations, defined by the orientation of successive benzopyrazine rings (Figure S13). The parallel conformation predominates in the chlorobenzene solution because it has a higher dipole moment (5.2 D) than the antiparallel conformation, which has a smaller dipole moment value (0.5 D).

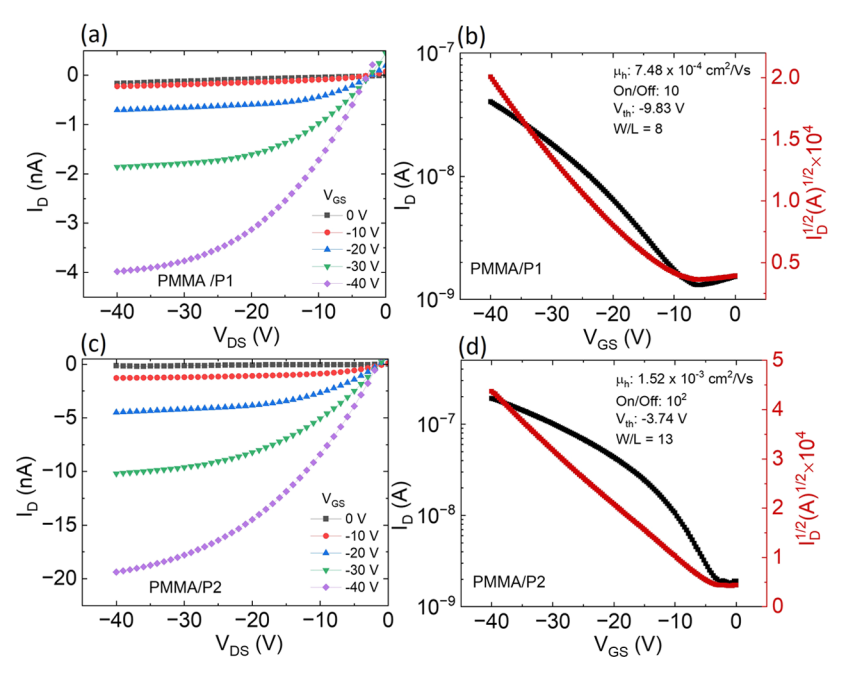


Figure 4. FET characteristics of top-gate FETs with PMMA as the dielectric layer. (a,b) Output and transfer current—voltage characteristics from a P1 FET, respectively. (c,d) Output and transfer current—voltage characteristics from a P2 FET, respectively.

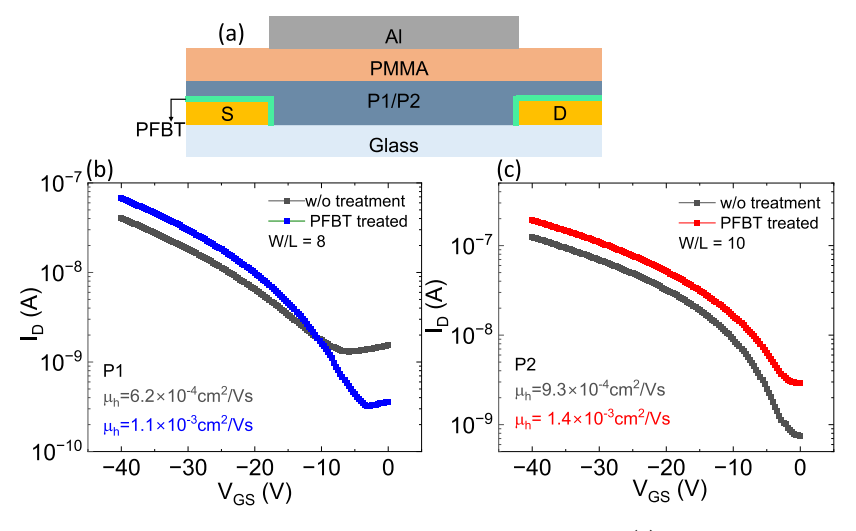


Figure 5. Transfer characteristics of top-gate P1/P2 FETs with PMMA as the dielectric layer. (a) Schematic of a FET with treated S/D contacts. (b) Transfer characteristics from two similar P1 FETs without the treatment of the S/D contacts (gray curve) and with the treatment of the S/D contacts (blue curve). (c) Transfer characteristics from two similar P2 FETs without the treatment of the S/D contacts (gray curve) and with the treatment of the S/D contacts (red curve).

Since the calculations are for a dimer, the difference between the HOMO and LUMO energy levels is higher compared with the experiment; however, the trend of a deeper LUMO level in P2 due to the electron-withdrawing pyridyl pyrazine units, as seen experimentally, is captured in theory as well. At variance with the experimental data, the HOMO level of P2 is at a less negative potential relative to P1. This discrepancy arises since P1 and P2 were calculated using dimeric and apparent tetrameric structures, respectively.

**3.3. FET Characteristics in Top-Gate and Bottom-Gate Architectures.** *3.3.1. With PMMA as the Top Gate.* Both top-gate and bottom-gate architecture FETs were fabricated. The advantage of the top-gate architecture is that the bottom-contacted Au source/drain contacts may be treated and that it allows for the dielectric layer to encapsulate the semiconductor

to shield it from potential degradation during device operation owing to the influences of ambient atmosphere. Figure 4 shows the output and transfer characteristics of TGBC-representative P1 and P2 FETs. For most devices, the S/D drain contacts were plasma-treated prior to depositing the semiconducting layer, which acts to chemically etch away organic contaminants and further clean the surfaces. Furthermore, it has been previously reported that the application of oxygen plasma to the surface of Au can act to form  ${\rm AuO}_x$  layers which can act to improve the injection of holes.

Treating the S/D contacts using a self-assembled monolayer of pentafluorobenzenethiol (PFBT) is observed to significantly improve the performance of P1 FETs compared with P2, as seen in Figure 5. This improvement of p-type transport through the introduction of a PFBT interlayer has been

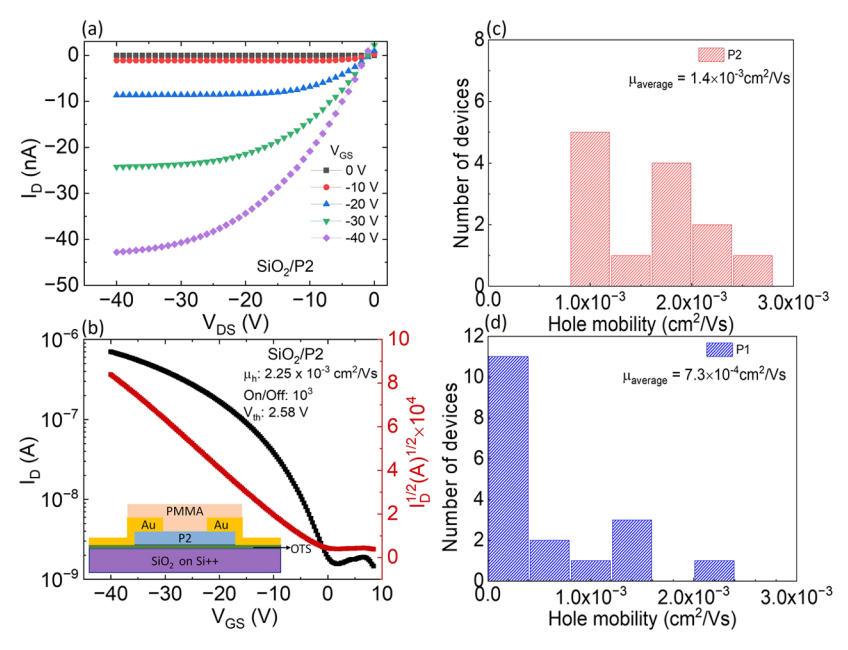


Figure 6. (a,b) Output and transfer characteristics of a BGTC P2 FET, respectively. The inset in (b) shows a schematic of the device. (c,d) Histograms of carrier mobilities from P1 and P2 FETs, respectively.

demonstrated previously for other materials.<sup>42</sup> The addition of the PFBT interlayer acts to lower the work function of gold. The difference in the impact of applying PFBT for each copolymer can be understood based on the differing HOMO levels of the two copolymers (Figure 2d). Unlike P1, the HOMO level of P2 is already close to that of the work function of Au (~-5.0 eV) without any treatment, so lowering it further through the introduction of the interlayer does not benefit charge injection. Hence, the SAM layer treatment of Au drives it closer to the HOMO level of P1 but further from the HOMO level of P2, resulting in only the former copolymer experiencing improved hole injection, especially with a higher on/off ratio.

There are several parameters that play a role for enhanced ptype transport: molecular weight, backbone coplanarity, appropriate HOMO-LUMO energy levels, and the film morphology and crystallinity. For Au S/D contacts, the ideal HOMO energy level should be between -5.0 and -5.5 eV, and the LUMO level should be higher than  $-3.5 \text{ eV.}^8$  The high off current in P1 (without any PFBT treatment) compared with that in P2 is likely due to the shallow HOMO level. Such shallow HOMO levels in p-type transport could result in pdoping in air, thus causing instability. The DPP-based copolymers with HOMO levels close to -5.2 eV tend to show better on/off ratios and air stability.9 With PFBT treatment, the HOMO level in P1 becomes deeper, and a clear decrease in the off current is seen. It is not exactly clear why the off current is slightly higher in P2 after the PFBT treatment. FETs with different W/L ratios, however, show the same trend that the SAM layer does not improve the overall performance in P2.

3.3.2. With SiO<sub>2</sub> as the Bottom Gate. We have further utilized the two copolymers in bottom-gate architectures with SiO<sub>2</sub> as the dielectric layer. A thin layer of PMMA was also applied to this architecture to serve as an encapsulant. Although this architecture shows an improved on/off ratio and subthreshold swing, the overall carrier mobility of the P1 FET in this architecture is lower (see Supporting Information)

compared to the top-gate architecture. Figure 6a,b shows the output and transfer characteristics of a  $SiO_2/P2$  FET. Figure 6c,d depicts the histograms of carrier mobilities from P1 and P2 FETs, which include both top-gate (with PMMA) and bottom-gate (with  $SiO_2$ ) architectures. It should be noted that for P1, more than 11 FETs show carrier mobilities lower than  $10^{-3}$  cm<sup>2</sup>/(V s), typically in the range of  $10^{-4}$  to  $10^{-5}$  cm<sup>2</sup>/(V s). The average FET carrier mobility of P2 is almost twice that of P1. The slightly improved performance of P2 FETs may be understood based on the planar polymer backbone structure due to the N-pyridyl atoms, as demonstrated by DFT calculations, facilitating an improved charge transport.

3.4. Complementary Voltage Inverter Circuits. A single p-type FET may be combined with a single n-type FET to form a simple, complementary logic architecture known as a voltage inverter circuit. A voltage inverter, utilizing an organic p-type and n-type FET, is the simplest example of a digital circuit.  $^{43-48}$  In the operation of an inverter circuit, an input voltage signal  $(V_{in})$  is applied to both FETs through a common gate contact. The "pull-up" FET (p-type device) is connected to a supply voltage  $(V_{
m DD})$ , and the "pull-down" FET (n-type device) is connected to the ground. The output voltage signal  $(V_{out})$  is then measured from a common drain contact shared between both devices. As the input voltage is swept, the circuit alternates between two steady logic states—one in which only the p-type FET is operational and one in which only the n-type FET is operational. For such a circuit, power is only consumed as it switches between the two steady states. As the supply voltage  $(V_{\rm DD})$  is increased step-by-step, the "trip point" and maximum  $V_{\text{out}}$  for each  $V_{\text{in}}$  sweep also increases. The trip point is defined as the point at which  $V_{in} = V_{out}$  during the voltage transfer characteristics and ideally should occur when  $V_{\rm in}$  is approximately equal to half the supply voltage for good noise margins. The signal gain for the circuit is related to the rate of change of the output as the input voltage is swept  $(\partial V_{\text{out}}/\partial V_{\text{in}})$ . Because the largest change occurs at the trip point, the gain is expected to peak at the associated voltage.

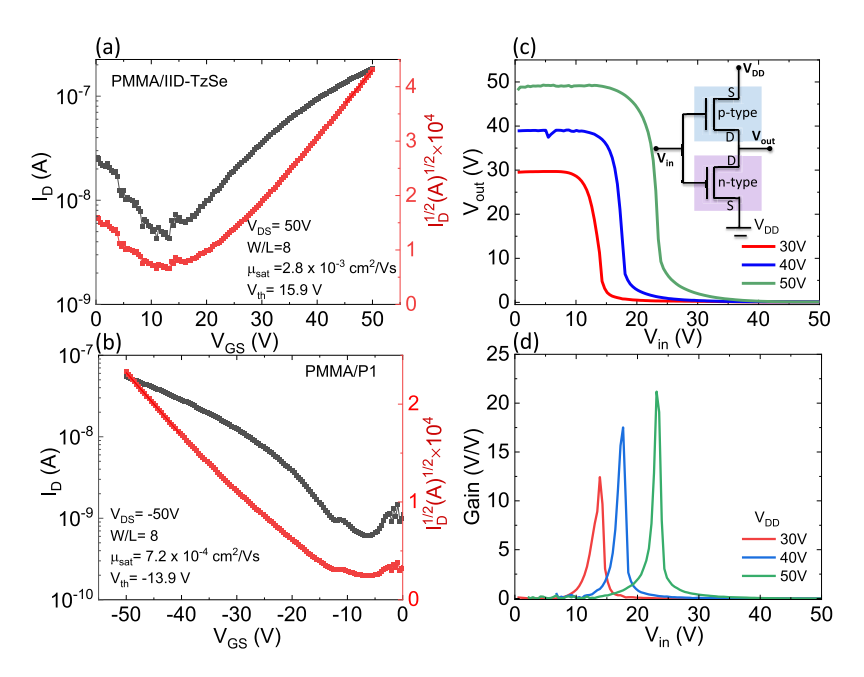


Figure 7. Inverter characteristics of IID-TzSe and P1. (a,b) Transfer characteristics of the individual IID-TzSe and P1 FETs, respectively. (c) Voltage transfer characteristics of the P1-IID-TzSe inverter circuit. The inset represents the schematic of the circuit layout. (d) Signal gain of the P1-IID-TzSe inverter.

We sought to construct proof-of-concept complementary inverters utilizing the P1 and P2 copolymers. To realize the ideal inverter operation, with strong signal gain and uniform noise margins, it is important that both FET devices used have equal magnitude currents throughout the operation. In this way, for the pull-down transistor, we needed to select a material for constructing an n-type FET which has similar operational characteristics to our P1 and P2 devices. We have previously demonstrated n-type behavior in a TGBC architecture for IID-TzSe FETs. <sup>17</sup> For such devices, an average electron mobility of  $1.8 \times 10^{-2}$  cm<sup>2</sup>/(V s) was demonstrated, with the results from nonlinear optical methods suggesting that mobilities as high as 0.25 cm<sup>2</sup>/(V s) could be achieved if the influences of contact resistance and interfacial trapping were removed.<sup>17</sup> As such, these devices can act complementary to the P1 and P2 devices considered thus far. Figure 7a,b outlines the individual FET characteristics of IID-TzSe and P1 FET devices, respectively. The output characteristics of these devices are shown in Supporting Information. The mobilities of each device are within one order of magnitude of each other, and there is only a difference of 2 V in the magnitude of each device's threshold voltages. The drain—source currents  $(I_D)$  for each device within saturation are comparable. We note that IID-TzSe used in this work has a different molecular weight compared with our prior work, 17 resulting in slightly lower carrier mobilities here.

Figure 7c demonstrates the voltage transfer characteristics (VTC) of the complementary P1-IID-TzSe inverter. Here, the trip point voltages for the 30, 40, and 50 V sweeps are 13.9, 17.6, and 23.1 V, respectively. The slight deviation of the trip point from the ideal value of  $V_{\rm DD}/2$  for each sweep can be understood as originating from the slight differences in the  $I_{\rm D}$  and  $V_{\rm Th}$  values for each device. The inverter shows distinct logic states, where  $V_{\rm out}$  is pulled up to  $V_{\rm DD}$  at low values of  $V_{\rm in}$  and subsequently pulled down fully to the ground at high values of  $V_{\rm in}$ , as expected. For the  $V_{\rm DD}$  = 50 V sweep, a promising maximum gain of 21 is observed.

Using an analytical model by Bode et al., 43 we have modeled the inverter characteristics of IID-TzSe and P1. The inverter characteristics requires five different regions for modeling. 49 The two extreme (regions 1 and 5) are (i)  $V_{\rm in} < V_{\rm Th}$  of the ntype FET,  $V_{\text{out}} = V_{\text{DD}}$  and (ii)  $V_{\text{in}} > V_{\text{Th}}$  (p-type) +  $V_{\text{DD}}$ ,  $V_{\text{out}} =$ 0. These two regions correspond to the p-type and n-type FETs being operational, respectively. The regions 2-4 rely on an analytical model, resulting in a cubic polynomial due to the equal and opposite current in the n-type and p-type FETs. The detailed equations for modeling are provided in Supporting Information. To predict the output characteristics of a voltage inverter, detailed characteristics of individual FETs in terms of  $\mu$  and  $V_{
m Th}$  are required. Additionally, the variation of the conductance ( $\lambda$ ) with  $V_{\rm DS}$  in the saturation region is also required. We first model the FET output curves by a unified model that was described by Estrada et al.,50 which takes both the linear and the saturation region together, and is given by

$$I_{\rm DS} = \frac{W}{L} C_{\rm i} \frac{\mu(V_{\rm GS} - V_{\rm T})}{\left(1 + R \frac{W}{L} C_{\rm i} \mu(V_{\rm GS} - V_{\rm T})\right)} \times \frac{V_{\rm DS}(1 + \lambda V_{\rm DS})}{\left[1 + \left[\frac{V_{\rm DS}}{V_{\rm DSsat}}\right]^{m}\right]^{1/m}} + I_{0}$$
(1)

In eq. 1, R is the drain source resistance,  $I_0$  is the leakage current, m is a fitting parameter describing the sharpness of the saturation region, and the saturation voltage:  $V_{\rm DSsat} = \alpha (V_{\rm GS} - V_{\rm Th})$  takes into account the modulation parameter,  $\alpha$ .

The fits to the n-type and p-type FET output curves are shown in Supporting Information for obtaining the above parameters required for modeling the inverter characteristics for the highest  $V_{\rm DD}$  = 50 V. The codes were written in scientific Python. Even though the fits to the output curve have discrepancies, the parameters obtained from the output characteristics predict the inverter characteristics quite well, and the simulated curve mimics our experimental data.

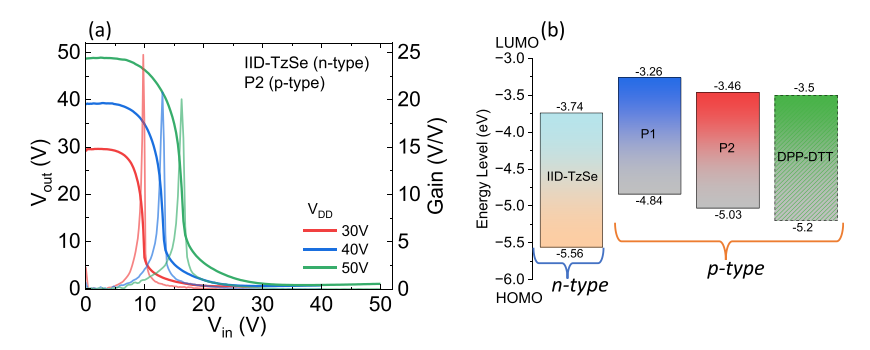


Figure 8. Inverter characteristics of IID-TzSe and P2. (a) Voltage transfer characteristics (left axis) and signal gain (right axis) of the P2-IID-TzSe inverter circuit. (b) Schematic of the HOMO/LUMO levels of the p-type (P1/P2 and DPP-DTT) and n-type (IID-TzSe) FET channels.

Voltage inverter circuits were also fabricated from P2 and IID-TzSe FETs. The VTC and gain are shown in Figure 8a. The FET characteristics of the individual devices are presented in Supporting Information. The P2 device, by comparison, has a lower magnitude mobility and a higher magnitude threshold voltage compared with the IID-TzSe device. These devices were similarly interconnected to form a complementary inverter architecture. The inverter is seen to reach its trip point at input voltages lower than the expected  $V_{\rm DD}/2$ . Here, the trip point voltages for the 30, 40, and 50 V sweeps are 9.8, 13.0, and 16.3 V, respectively. The deviation from  $V_{\rm DD}/2$  here is due to the difference in threshold voltages between the two FETs. Because  $V_{\mathrm{Th}}$  for the n-type device (IID-TzSe) is much lower than that of the p-type device P2, the n-type device turns on at lower values of  $V_{\rm in}$ , and the inverter begins to switch between the steady logic states sooner. This inverter also shows the expected logic states where  $V_{\text{out}}$  is pulled up to  $V_{\text{DD}}$ at low values of  $V_{in}$  and subsequently pulled down fully to the ground at high values of  $V_{\rm in}$ . For the  $V_{\rm DD}$  = 50 V sweep, a maximum gain of 20 is observed. It is important to realize that the difference in the HOMO levels between IID-TzSe and P2 is lower than that between IID-TzSe and P1 (Figure 8b), which may result in minority carrier (holes in the case of IID-TzSe)-induced parasitic currents, affecting both the trip point and the gain.

To obtain further insights into the differences in the inverter characteristics of P1 and P2 with IID-TzSe, we selected DPP-DTT (dithienylthieno[3,2-b]thiophene (DTT)-based DPP) with a deeper HOMO level compared with P2 in an inverter circuit with IID-TzSe. We note that DPP-DTT demonstrates mostly a p-type behavior. These results are presented in Supporting Information. Although the gain (30) is larger compared with the P1 or P2 FETs, the trip point is shifted to slightly higher values, and with increasing  $V_{\rm in}$ ,  $V_{\rm out}$  begins to be pulled up. Such a shift in  $V_{\rm out}$  is due to the influence of the DPP-DTT device, which is still ambipolar and likely not completely "off" in this state. These observations with the DPP-DTT and IID-TzSe inverter suggest that the difference in  $V_{\rm Th}$  between the IID-TzSe and the P2 FET is a likely reason for lowering the trip point compared with the ideal condition. A comparison of the three inverter circuits shows that even with modest performance, P1 or P2 FETs have potential applications in digital circuits when combined with other D-A copolymers such as IIDs.

A comparison of the three inverter circuits along with analytical modeling provides insights into the FET parameters of the n- and p-type FETs that dictate the overall characteristics. Even if the overall carrier mobilities are low, similar  $V_{\rm Th}$ 

for the n- and p-type FETs ensures that the trip point is at  $V_{\rm DD}/2$  with a gain of over 20. The relative widths (w) of the pand n-type FETs are inversely proportional to the currents

through the devices  $\left(\frac{W_p}{W_n} = \frac{I_n}{I_p}\right)$ . Altering the size of each device

shifts the trip point in inverter voltage characteristics. For submicron complementary inverter devices, it is typical for the ratio of current through the n-type device  $(I_n)$  to that of the ptype device  $(I_p)$  to be 2.<sup>51</sup> Along with the actual n- and p-type FET characteristics, the HOMO/LUMO offsets between the n-type and p-type semiconductors play a role. The inverter characteristics of DPP-DTT/IID-TzSe demonstrate that the difference between the LUMO energy of the two materials should be > 0.24 eV; otherwise, with an increase in  $V_{\rm in}$ ,  $V_{\rm out}$ begins to be pulled up.

### 4. CONCLUSIONS

This work demonstrated the synthesis and characterization of two TVT-based copolymers, one of them being regioregular with the presence of an additional electronegative N atom (P2). The inclusion of the N atom in P2 further lowers the HOMO and LUMO energy levels compared with P1. When utilized in staggered FET architectures (BGTC and TGBC), P2 demonstrated higher hole mobilities on average compared to that of P1, which may be understood on the basis of a planar conjugated backbone in P2. Using Au as the contact material for charge injection, both materials demonstrated a predominately p-type behavior, and, in the case of P1, treatment of the contacts with a PFBT monolayer was observed to further enhance the device performance due to the modification of the contact work function of Au. As the HOMO level of **P2** is already close to the work function of Au, such modifications were not observed to impart any further benefit to the device performance.

Both copolymer-based FET devices were also demonstrated to provide promising complementary logic in voltage inverter circuits constructed using IID-TzSe based FETs as the pulldown transistor. The inverter using the P1 FET as the pull-up transistor showed a slightly higher gain and more uniform noise margins (owing to the closeness of the trip point to  $V_{\rm DD}/$ 2) than that with the P2 FET. Both circuits showed steady logic states, with no noticeable influence of minority carriers on the output voltage at very high or very low input voltages.

Designing copolymers of Qx and PyPyz with coplanar donor units such as TVT tunes the optical and electrochemical band gap energies for their application not just in thin-film transistors, but combining with other D-A IID-based n-type FETs has promising applications in digital electronic circuits.

#### ASSOCIATED CONTENT

## **5** Supporting Information

The Supporting Information is available free of charge at https://pubs.acs.org/doi/10.1021/acsaelm.3c01790.

Synthesis procedure of polymers, NMR characterization, GPC, thermogravimetric analysis, X-ray diffraction, atomic force microscopy analysis, field-effect transistor characteristics with SiO<sub>2</sub> gate dielectric, representative transfer characteristics with gate leakage current, inverter modeling and parameters, inverter characteristics, and polymer conformations (PDF)

## AUTHOR INFORMATION

## **Corresponding Authors**

Mohammed Al-Hashimi — Department of Chemical Engineering, Texas A&M University at Qatar, Doha 23874, Qatar; ⊙ orcid.org/0000-0001-6015-2178; Email: mohammed.al-hashimi@tamu.edu

Suchismita Guha — Department of Physics and Astronomy, University of Missouri, Columbia, Missouri 65211, United States; orcid.org/0000-0002-6269-2298; Email: guhas@ missouri.edu

#### **Authors**

John Barron – Department of Physics and Astronomy, University of Missouri, Columbia, Missouri 65211, United States

Salahuddin Attar — Department of Chemical Engineering, Texas A&M University at Qatar, Doha 23874, Qatar; o orcid.org/0000-0003-1341-2218

Arash Ghobadi — Department of Physics and Astronomy, University of Missouri, Columbia, Missouri 65211, United States

Shubhra Gangopadhyay — Department of Electrical Engineering and Computer Science, University of Missouri, Columbia, Missouri 65211, United States

Dusan Sredojevic — Vinča Institute of Nuclear Sciences, National Institute of the Republic of Serbia, University of Belgrade, Centre of Excellence for Photoconversion, Belgrade 11001, Serbia; orcid.org/0000-0003-2867-2047

Complete contact information is available at: https://pubs.acs.org/10.1021/acsaelm.3c01790

# **Author Contributions**

J.B. and S.A. have contributed equally to this work. S.G. and M.Al-H. conceived the work. S.A. and M.Al-H. carried out the synthesis and characterization of the copolymers. J.B. and A.G. were involved with device fabrication and characterization. S.G. and S.G. helped with the analysis of the device characterization and setup. D.S. carried out the DFT calculations. The manuscript was written by S.G., J.B., and S.A. through contributions of all authors. All authors have given approval to the final version of the manuscript.

#### Notes

The authors declare no competing financial interest.

## ACKNOWLEDGMENTS

We acknowledge partial support of this work through the U.S. National Science Foundation (NSF) under grant no. ECCS-2324839 and Qatar National Research Fund (QNRF) and the National Priorities Research Program (project number NPRP12S-0304-190227).

#### REFERENCES

- (1) Wang, C.; Dong, H.; Hu, W.; Liu, Y.; Zhu, D. Semiconducting Π-Conjugated Systems in Field-Effect Transistors: A Material Odyssey of Organic Electronics. *Chem. Rev.* **2012**, *112*, 2208–2267.
- (2) Facchetti, A. Π-Conjugated Polymers for Organic Electronics and Photovoltaic Cell Applications. *Chem. Mater.* **2011**, 23, 733–758.
- (3) Müllen, K.; Pisula, W. Donor-Acceptor Polymers. J. Am. Chem. Soc. 2015, 137, 9503–9505.
- (4) Paterson, A. F.; Singh, S.; Fallon, K. J.; Hodsden, T.; Han, Y.; Schroeder, B. C.; Bronstein, H.; Heeney, M.; McCulloch, I.; Anthopoulos, T. D. Recent Progress in High-Mobility Organic Transistors: A Reality Check. *Adv. Mater.* **2018**, *30*, 1801079.
- (5) Kim, M.; Ryu, S. U.; Park, S. A.; Choi, K.; Kim, T.; Chung, D.; Park, T. Donor-Acceptor-Conjugated Polymer for High-Performance Organic Field-Effect Transistors: A Progress Report. *Adv. Funct. Mater.* **2020**, *30*, 1904545.
- (6) Pandey, L.; Risko, C.; Norton, J. E.; Brédas, J. L. Donor-Acceptor Copolymers of Relevance for Organic Photovoltaics: A Theoretical Investigation of the Impact of Chemical Structure Modifications on the Electronic and Optical Properties. *Macromolecules* **2012**, *45*, 6405–6414.
- (7) Wang, J.; Jiang, X.; Wu, H.; Feng, G.; Wu, H.; Li, J.; Yi, Y.; Feng, X.; Ma, Z.; Li, W.; Vandewal, K.; Tang, Z. Increasing Donor-Acceptor Spacing for Reduced Voltage Loss in Organic Solar Cells. *Nat. Commun.* **2021**, *12*, 6679.
- (8) Yang, J.; Zhao, Z.; Wang, S.; Guo, Y.; Liu, Y. Insight into High-Performance Conjugated Polymers for Organic Field-Effect Transistors. *Chem* **2018**, *4*, 2748–2785.
- (9) Lee, H. W.; Kim, H. S.; Kim, D.; Yoon, M.; Lee, J.; Hwang, D.-H. Comparative Study of Charge-Transport Behavior of Edge-on- and Face-on-Oriented Diketopyrrolopyrrole-Based Conjugated Copolymers Bearing Chalcogenophene Units. *Chem. Mater.* **2022**, *34*, 314–324.
- (10) Mukhopadhyay, T.; Puttaraju, B.; Senanayak, S. P.; Sadhanala, A.; Friend, R.; Faber, H. A.; Anthopoulos, T. D.; Salzner, U.; Meyer, A.; Patil, S. Air-Stable N-Channel Diketopyrrolopyrrole-Diketopyrrolopyrrole Oligomers for High Performance Ambipolar Organic Transistors. ACS Appl. Mater. Interfaces 2016, 8, 25415—25427.
- (11) Liu, J.; Sun, Y.; Moonsin, P.; Kuik, M.; Proctor, C. M.; Lin, J.; Hsu, B. B.; Promarak, V.; Heeger, A. J.; Nguyen, T.-Q. Tri-Diketopyrrolopyrrole Molecular Donor Materials for High-Performance Solution-Processed Bulk Heterojunction Solar Cells. *Adv. Mater.* **2013**, 25, 5898–5903.
- (12) Pickett, A.; Mohapatra, A.; Laudari, A.; Khanra, S.; Ram, T.; Patil, S.; Guha, S. Hybrid Zno-Organic Semiconductor Interfaces in Photodetectors: A Comparison of Two near-Infrared Donor-Acceptor Copolymers. *Org. Electron.* **2017**, *45*, 115–123.
- (13) Attar, S.; Yang, R.; Chen, Z.; Ji, X.; Comí, M.; Banerjee, S.; Fang, L.; Liu, Y.; Al-Hashimi, M. Thiazole Fused S,N-Heteroacene Step-Ladder Polymeric Semiconductors for Organic Transistors. *Chem. Sci.* 2022, *13*, 12034–12044.
- (14) Al-Hashimi, M.; Han, Y.; Smith, J.; Bazzi, H. S.; Alqaradawi, S. Y. A.; Watkins, S. E.; Anthopoulos, T. D.; Heeney, M. Influence of the Heteroatom on the Optoelectronic Properties and Transistor Performance of Soluble Thiophene-Selenophene- and Tellurophene-Vinylene Copolymers. *Chem. Sci.* **2016**, *7*, 1093–1099.
- (15) Lei, T.; Dou, J.-H.; Ma, Z.-J.; Yao, C.-H.; Liu, C.-J.; Wang, J.-Y.; Pei, J. Ambipolar Polymer Field-Effect Transistors Based on Fluorinated Isoindigo: High Performance and Improved Ambient Stability. J. Am. Chem. Soc. 2012, 134, 20025–20028.
- (16) Park, K. H.; Cheon, K. H.; Lee, Y.-J.; Chung, D. S.; Kwon, S.-K.; Kim, Y.-H. Isoindigo-Based Polymer Field-Effect Transistors: Effects of Selenophene-Substitution on High Charge Carrier Mobility. *Chem. Commun.* **2015**, *51*, 8120–8122.
- (17) Barron, J.; Attar, S.; Bhattacharya, P.; Yu, P.; Al-Hashimi, M.; Guha, S. Visualizing Transport in Thiazole Flanked Isoindigo-Based Donor-Acceptor Polymer Field-Effect Transistors. *J. Mater. Chem. C* **2022**, *10*, 14653–14660.

- (18) Kiefer, D.; Giovannitti, A.; Sun, H.; Biskup, T.; Hofmann, A.; Koopmans, M.; Cendra, C.; Weber, S.; Anton Koster, L. J.; Olsson, E.; Rivnay, J.; Fabiano, S.; McCulloch, I.; Müller, C. Enhanced N-Doping Efficiency of a Naphthalenediimide-Based Copolymer through Polar Side Chains for Organic Thermoelectrics. *ACS Energy Lett.* **2018**, 3, 278–285.
- (19) Chang, Y.; Wu, Y.-S.; Tung, S.-H.; Chen, W.-C.; Chueh, C.-C.; Liu, C.-L. N-Type Doping of Naphthalenediimide-Based Random Donor-Acceptor Copolymers to Enhance Transistor Performance and Structural Crystallinity. ACS Appl. Mater. Interfaces 2023, 15, 15745—15757.
- (20) Cassinelli, M.; Cimò, S.; Biskup, T.; Jiao, X.; Luzio, A.; McNeill, C. R.; Noh, Y.-Y.; Kim, Y.-H.; Bertarelli, C.; Caironi, M. Enhanced N-Type Doping of a Naphthalene Diimide Based Copolymer by Modification of the Donor Unit. *Adv. Electron. Mater.* **2021**, *7*, 2100407.
- (21) Wang, Y.; Michinobu, T. Benzothiadiazole and Its II-Extended, Heteroannulated Derivatives: Useful Acceptor Building Blocks for High-Performance Donor-Acceptor Polymers in Organic Electronics. *J. Mater. Chem. C* **2016**, *4*, 6200–6214.
- (22) Dutta, G. K.; Guha, S.; Patil, S. Synthesis of Liquid Crystalline Benzothiazole Based Derivatives: A Study of Their Optical and Electrical Properties. *Org. Electron.* **2010**, *11*, 1–9.
- (23) Sun, C.; Zhu, C.; Meng, L.; Li, Y. Quinoxaline-Based D-a Copolymers for the Applications as Polymer Donor and Hole Transport Material in Polymer/Perovskite Solar Cells. *Adv. Mater.* **2022**, *34*, 2104161.
- (24) Gedefaw, D.; Prosa, M.; Bolognesi, M.; Seri, M.; Andersson, M. R. Recent Development of Quinoxaline Based Polymers/Small Molecules for Organic Photovoltaics. *Adv. Energy Mater.* **2017**, *7*, 1700575.
- (25) Zhao, Z.; Zhang, Y.; Wang, Y.; Qin, X.; Wu, J.; Hou, J. Fluorinated and Non-Fluorinated Conjugated Polymers Showing Different Photovoltaic Properties in Polymer Solar Cells with Pfnbr Interlayers. *Org. Electron.* **2016**, *28*, 178–183.
- (26) Cui, Y.; Xu, Y.; Yao, H.; Bi, P.; Hong, L.; Zhang, J.; Zu, Y.; Zhang, T.; Qin, J.; Ren, J.; Chen, Z.; He, C.; Hao, X.; Wei, Z.; Hou, J. Single-Junction Organic Photovoltaic Cell with 19% Efficiency. *Adv. Mater.* **2021**, 33, 2102420.
- (27) Dai, Z.; Zhang, D.; Zhang, H. Design, Synthesis, and Application in Ofet of a Quinoxaline-Based D-a Conjugated Polymer. *Front. Chem.* **2022**, *10*, 934203.
- (28) Jang, S.-Y.; Lim, B.; Yu, B.-K.; Kim, J.; Baeg, K.-J.; Khim, D.; Kim, D.-Y. Synthesis and Characterization of Low-Band-Gap Poly(Thienylenevinylene) Derivatives for Polymer Solar Cells. *J. Mater. Chem.* **2011**, *21*, 11822–11830.
- (29) Lee, M.-H.; Kim, J.; Kang, M.; Kim, J.; Kang, B.; Hwang, H.; Cho, K.; Kim, D.-Y. Precise Side-Chain Engineering of Thienylene-vinylene-Benzotriazole-Based Conjugated Polymers with Coplanar Backbone for Organic Field Effect Transistors and Cmos-Like Inverters. ACS Appl. Mater. Interfaces 2017, 9, 2758–2766.
- (30) Ying, L.; Hsu, B. B. Y.; Zhan, H.; Welch, G. C.; Zalar, P.; Perez, L. A.; Kramer, E. J.; Nguyen, T.-Q.; Heeger, A. J.; Wong, W.-Y.; Bazan, G. C. Regioregular Pyridal [2,1,3] Thiadiazole Π-Conjugated Copolymers. J. Am. Chem. Soc. 2011, 133, 18538–18541.
- (31) Zhu, C.; Zhao, Z.; Chen, H.; Zheng, L.; Li, X.; Chen, J.; Sun, Y.; Liu, F.; Guo, Y.; Liu, Y. Regioregular Bis-Pyridal[2,1,3]-Thiadiazole-Based Semiconducting Polymer for High-Performance Ambipolar Transistors. *J. Am. Chem. Soc.* **2017**, *139*, 17735–17738.
- (32) Ying, L.; Huang, F.; Bazan, G. C. Regioregular Narrow-Bandgap-Conjugated Polymers for Plastic Electronics. *Nat. Commun.* **2017**, *8*, 14047.
- (33) Kline, R. J.; McGehee, M. D.; Kadnikova, E. N.; Liu, J.; Fréchet, J. M. J.; Toney, M. F. Dependence of Regioregular Poly(3-Hexylthiophene) Film Morphology and Field-Effect Mobility on Molecular Weight. *Macromolecules* **2005**, *38*, 3312–3319.
- (34) Lee, B.-L.; Yamamoto, T. Syntheses of New Alternating Ct-Type Copolymers of Thiophene and Pyrido[3,4-B]Pyrazine Units: Their Optical and Electrochemical Properties in Comparison with

- Similar Ct Copolymers of Thiophene with Pyridine and Quinoxaline. *Macromolecules* **1999**, 32, 1375–1382.
- (35) Hestand, N. J.; Spano, F. C. Expanded Theory of H- and J-Molecular Aggregates: The Effects of Vibronic Coupling and Intermolecular Charge Transfer. *Chem. Rev.* **2018**, *118*, 7069–7163.
- (36) Becke, A. D. Density-Functional Thermochemistry. Iii. The Role of Exact Exchange. *J. Chem. Phys.* **1993**, *98*, 5648–5652.
- (37) Lee, C.; Yang, W.; Parr, R. G. Development of the Colle-Salvetti Correlation-Energy Formula into a Functional of the Electron Density. *Phys. Rev. B* **1988**, *37*, 785–789.
- (38) Ditchfield, R.; Hehre, W. J.; Pople, J. A. Self-Consistent Molecular-Orbital Methods. Ix. An Extended Gaussian-Type Basis for Molecular-Orbital Studies of Organic Molecules. *J. Chem. Phys.* **1971**, 54, 724–728.
- (39) Frisch, M.; Trucks, G.; Schlegel, H.; Scuseria, G.; Robb, M.; Cheeseman, J.; Scalmani, G.; Barone, V.; Mennucci, B.; Petersson, G.; Nakatsuji, H.; Caricato, M.; Li, X.; Hratchian, H.; Izmaylov, A.; Bloino, J.; Zheng, G.; Sonnenberg, J.; Hada, M.; Fox, D. Gaussian 09 (Revision A02); Gaussian Inc: Wallingford CT, 2009.
- (40) Bondi, A. Van Der Waals Volumes and Radii. J. Phys. Chem. 1964, 68, 441-451.
- (41) Stadlober, B.; Haas, U.; Gold, H.; Haase, A.; Jakopic, G.; Leising, G.; Koch, N.; Rentenberger, S.; Zojer, E. Orders-of-Magnitude Reduction of the Contact Resistance in Short-Channel Hot Embossed Organic Thin Film Transistors by Oxidative Treatment of Au-Electrodes. *Adv. Funct. Mater.* 2007, 17, 2687–2692.
- (42) Borchert, J. W.; Weitz, R. T.; Ludwigs, S.; Klauk, H. A Critical Outlook for the Pursuit of Lower Contact Resistance in Organic Transistors. *Adv. Mater.* **2022**, *34*, 2104075.
- (43) Bode, D.; Rolin, C.; Schols, S.; Debucquoy, M.; Steudel, S.; Gelinck, G. H.; Genoe, J.; Heremans, P. Noise-Margin Analysis for Organic Thin-Film Complementary Technology. *IEEE Trans. Electron Devices* **2010**, *57*, 201–208.
- (44) Jung, S.; Kwon, J.; Tokito, S.; Horowitz, G.; Bonnassieux, Y.; Jung, S. Compact Modelling and Spice Simulation for Three-Dimensional, Inkjet-Printed Organic Transistors, Inverters and Ring Oscillators. *J. Phys. D: Appl. Phys.* **2019**, *52*, 444005.
- (45) Opitz, A.; Bronner, M.; Brütting, W. Ambipolar Charge Carrier Transport in Mixed Organic Layers of Phthalocyanine and Fullerene. *J. Appl. Phys.* **2007**, *101*, 063709.
- (46) Petritz, A.; Krammer, M.; Sauter, E.; Gärtner, M.; Nascimbeni, G.; Schrode, B.; Fian, A.; Gold, H.; Cojocaru, A.; Karner-Petritz, E.; et al. Embedded Dipole Self-Assembled Monolayers for Contact Resistance Tuning in P-Type and N-Type Organic Thin Film Transistors and Flexible Electronic Circuits. *Adv. Funct. Mater.* **2018**, 28, 1804462.
- (47) Uno, M.; Kanaoka, Y.; Cha, B. S.; Isahaya, N.; Sakai, M.; Matsui, H.; Mitsui, C.; Okamoto, T.; Takeya, J.; Kato, T.; et al. Short-Channel Solution-Processed Organic Semiconductor Transistors and Their Application in High-Speed Organic Complementary Circuits and Organic Rectifiers. *Adv. Electron. Mater.* **2015**, *1*, 1500178.
- (48) Yan, H.; Chen, Z.; Zheng, Y.; Newman, C.; Quinn, J. R.; Dötz, F.; Kastler, M.; Facchetti, A. A High-Mobility Electron-Transporting Polymer for Printed Transistors. *Nature* **2009**, 457, 679–686.
- (49) Barron, J.; Pickett, A.; Glaser, J.; Guha, S. Solution-Processed Organic and Zno Field-Effect Transistors in Complementary Circuits. *Electron. Mater.* **2021**, *2*, 60–71.
- (50) Estrada, M.; Cerdeira, A.; Puigdollers, J.; Reséndiz, L.; Pallares, J.; Marsal, L. F.; Voz, C.; Iñiguez, B. Accurate Modeling and Parameter Extraction Method for Organic Tfts. *Solid-State Electron.* **2005**, *49*, 1009–1016.
- (51) Taur, Y.; Ning, T. H. Fundamentals of Modern VLSI Devices; Cambridge University Press, 2021.